On the Modeling and Analysis of Machining Performance in Micro-Endmilling, Part II: Cutting Force Prediction

Michael P. Vogler[1]
Graduate Student

Shiv G. Kapoor
Professor,
Fellow ASME

Richard E. DeVor
Professor,
Fellow ASME

Department of Mechanical and Industrial Engineering,
University of Illinois at Urbana-Champaign,
Urbana, IL 61801-2906

In Part II of this paper, a cutting force model for the micro-endmilling process is developed. This model incorporates the minimum chip thickness concept in order to predict the effects of the cutter edge radius on the cutting forces. A new chip thickness computation algorithm is developed to include the minimum chip thickness effect. A slip-line plasticity force model is used to predict the force when the chip thickness is greater than the minimum chip thickness, and an elastic deformation force model is employed when the chip thickness is less than the minimum chip thickness. Orthogonal, microstructure-level finite element simulations are used to calibrate the parameters of the force models for the primary metallurgical phases, ferrite and pearlite, of multiphase ductile iron workpieces. The model is able to predict the magnitudes of the forces for both the ferrite and pearlite workpieces as well as for the ductile iron workpieces within 20%.
[DOI: 10.1115/1.1813471]

1 Introduction

As the endmilling process is miniaturized, the ratio between the chip thickness and the cutter edge radius changes, and the chip formation mechanics change significantly. In particular, no chip will be formed if the chip thickness is below the minimum chip thickness for the cutter edge radius-workpiece material pair. In Part I of this paper [1], this change in the chip formation process was characterized by the minimum chip thickness and was found to have a significant effect on the surface generation process in micro-endmilling. Besides the effect that the minimum chip thickness has on the surface generation, it will also have a significant effect on the cutting forces.

In addition to the size scaling that is present in micromilling between the cutter edge radius and the chip thickness, the relative size scales between the workpiece microstructure and chipload change. In our earlier work [2], we enhanced previous mechanistic force models to accommodate the prediction of cutting forces in multiphase materials. In the micromilling force model, a mapping of the workpiece microstructure is first performed. With the increments in time, the workpiece microstructural phase in which the cutting edges are located is determined for each axial slice of the endmill, and the chip thickness is determined. Equivalent orthogonal force components are computed for each slice and transformed into the Cartesian coordinate system where they are integrated to produce the force components for that time step. Although the previous model is able to account for the magnitude and variation of the forces for a given cutter edge radius through the calibration process employed in that work, it is unable to explicitly account for the scaling effects of the cutting edge radius and the chip thickness on the force system.

In Part II, the previous micro-endmilling force model will be enhanced by incorporating two effects of the cutter edge radius. First, the minimum chip thickness effect will be considered. This effect will require a modified chip thickness computation algorithm in order to account for the minimum chip thickness phenomenon in the chip formation process. Furthermore, the minimum chip thickness results in two separate force generation mechanisms, which must be modeled. The slip-line plasticity model developed by Waldorf et al. [3] is used here to model the shearing and ploughing forces in instances in which a chip is formed. When no chip is formed, elastic deformation forces are modeled as proportional to the interference volume similar in principle to the approach undertaken by Wu [4] and Endres et al. [5]. Both of these approaches explicitly include the cutter edge radius in the modeling. The force model will be calibrated for the single-phase ferrite and pearlite materials through application of finite element (FE) simulations. Finally, micromilling experiments will be presented that validate the force model over a range of processing conditions for both the single-phase and the multiphase ductile iron workpiece materials.

2 Model Development

To model the micromilling of heterogeneous materials, a mapping of the metallurgical phases must be created that represents the actual microstructure. In general, the number of phases that can be handled by the model is unlimited. In this study, the microstructure of ductile iron is modeled by considering the secondary (ferrite) and tertiary (graphite) phases to be spherical in shape. The mapping of the microstructure is developed in a three-step process described in Vogler et al. [2].

In order to handle machining through different phases simultaneously, the end mill is discretized into axial slices as shown in Fig. 1. The position of the cutting edge of the jth slice, (x_{Fj}, y_{Fj}, z_{Fj}), is calculated at each time step in the simulation for every flute engaged in the workpiece. This position is compared with the location of the spheres centered at (X_i, Y_i, Z_i) used to represent the grain structure in the model. If

$$R_{3i} < \sqrt{(x_{Fj}-X_i)^2+(y_{Fj}-Y_i)^2+(z_{Fj}-Z_i)^2}$$
$$i = 1, \ldots, N_{spheres} \qquad (1)$$
$$j = 1, \ldots, N_{slices}$$

where R_{3i} is the radius of the sphere representing the tertiary phase, then the cutting edge is located in the tertiary phase, and,

[1]Currently with Delphi Research Labs, Shelby Township, MI.

Contributed by the Manufacturing Engineering Division for publication in the JOURNAL OF MANUFACTURING SCIENCE AND ENGINEERING. Manuscript received February, 2003; revised March, 2004. Associate Editor: K. F. Ehman.

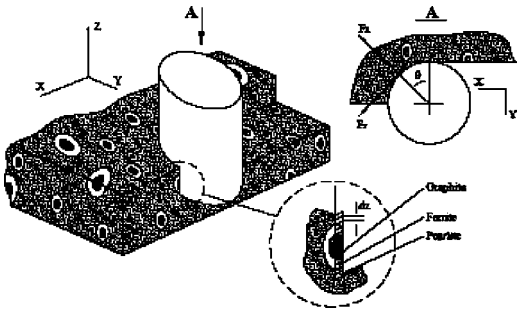

Fig. 1 Endmilling of ductile iron workpiece [1]

therefore, the force model for the tertiary phase is used. If the cutting edge is not in the tertiary phase for any of the spheres, then the cutting-edge location is compared to the secondary phase in a similar manner. If the cutting edge is located in neither the secondary nor tertiary phases, then the force model for the primary phase is used.

2.1 Chip Thickness Computation. In micromilling, due to the relative size scales of the cutter edge radius and chip thickness, it has been found that there exists a minimum chip thickness below which no chip will form [6–8], unlike in conventionally sized endmilling processes. In order to accurately compute the chip thickness in the presence of this phenomenon, a new procedure is required. Due to the fact that a chip is not always formed along the tool path, those portions of the tool path during which a chip was formed must be distinguished from those segments for which no chip was formed. In this work, those segments of the *i*th tool pass for which a chip was formed are distinguished by storing the angular locations of the start and end of chip formation as θ_{Si} and θ_{Ei}, respectively.

The algorithm used to compute the chip thickness consists of the following steps. First, the rotation angle, θ_{Fi}, of flute f_N ($f_N = 0,1,\ldots N-1$) during the *i*th tool pass is computed as

$$\theta_{Fi} = \theta - \frac{2f_N\pi}{N} - \delta\theta(z_{Fj}) \tag{2}$$

where $\theta = 2\pi RPMt/60$, and $\delta\theta(z_{Fj})$ is the additional angle that must be considered as the cutting edge rotates along the helix angle β, as the z coordinate is changed,

$$\delta\theta(z_F) = \frac{\tan\beta}{R} z_F \tag{3}$$

where R is the radius of the endmill. The coordinates of the tool center, (x_{Ci}, y_{Ci}), in the presence of runout can be computed as

$$x_{Ci} = \frac{Nf_t\theta}{2\pi} + r_o \sin(\theta - \lambda)$$
$$y_{Ci} = r_o \cos(\theta - \lambda) \tag{4}$$

where N is the number of flutes, f_t is the feed per flute, r_o is the magnitude of the parallel axis offset, and λ is the locating angle of the parallel axis offset. The coordinates of the cutting edge, (x_{Fi}, y_{Fi}), can then be computed as

$$x_{Fi}(j) = x_C(\theta) + R\sin\theta_{Fi}$$
$$y_{Fi}(j) = y_C(\theta) + R\cos\theta_{Fi} \tag{5}$$

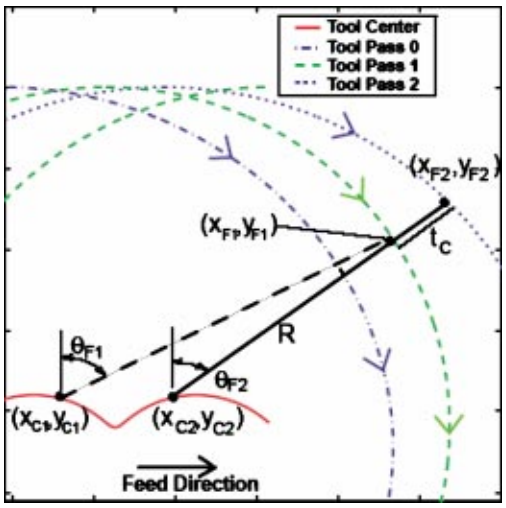

Fig. 2 Illustration of chip thickness computation

Then, beginning with the tool pass 0, the rotation angle θ_0 that results in the cutting edge F_0 intersecting the line connecting the tool center and the cutting edge of the *i*th tool pass, can be determined using Eqs. (4) and (5) for the $i=0$ tool pass. This value of θ_{F0} is then compared to the start and end values of θ, θ_{S0}, and θ_{E0}, for the zeroth tool pass, which defines the workpiece surface. If $\theta_{S0} \leqslant \theta_{F0} \leqslant \theta_{E0}$, then the current flute is intersecting the surface produced from the zeroth tool pass and the chip thickness for this tool pass is computed

$$t_C = R - \sqrt{(x_{F0} - x_{Ci})^2 + (y_{F0} - y_{Ci})^2} \tag{6}$$

If the computed value of t_C from Eq. (6) is greater than the minimum chip thickness value for the tool and workpiece combination, then the surface is modified for both the current (*i*th) tool pass and the zeroth tool pass. The current angular location θ_{Fi} is added to the workpiece surface, and the angular location for the previous tool pass θ_{F0} is removed from the workpiece surface. If the value of θ_{F0} does not lie on the surface for the zeroth tool pass, then the procedure is repeated for the next tool pass until either an intersection has been found or until all tool passes have been tried. The above coordinates are illustrated in Fig. 2 for 1.5 revolutions with a two-fluted endmill.

This procedure is illustrated in Figs. 3(*a*)–(*d*). At the start of tool pass 2 [Fig. 3(*a*)], the surface is composed of the solid arc segments from tool pass 0, S_0E_0, and from tool pass 1, S_1E_1. The intersection of the line connecting the current tool center to the cutter-edge location (x_{F2}, y_{F2}) and the arc S_0E_0 is then computed by solving Eq. (5) for the θ_{F0} that results in (x_{F0}, y_{F0}) lying on the line. For the value of the θ_{F0} shown in the Fig. 3(*a*), the chip thickness is computed using Eq. (6) and compared to the minimum chip thickness. For this situation, it is assumed that the chip thickness is smaller than the minimum chip thickness.

Figure 3(*b*) shows the process after a few time steps. Now, the workpiece surface is comprised of the arc segments $S_{0,1}E_{0,1}$, and $S_{0,2}E_{0,2}$ from tool pass 0, arc segments S_1E_1 from tool pass 1, and the newly generated surface S_2E_2. As the cutting edge reached point S_2, the chip thickness between the current tool pass and tool pass 0 became larger than the minimum chip thickness. The previous workpiece surface was then modified by splitting the existing surface into two segments, $S_{0,1}E_{0,1}$ and $S_{0,2}E_{0,2}$. As the cutting edge progresses, the surface arc segment $S_{0,2}E_{0,2}$ is swept away until the condition in Fig. 3(*c*) is reached. Also, a newly generated surface is being created as arc segment S_2E_2.

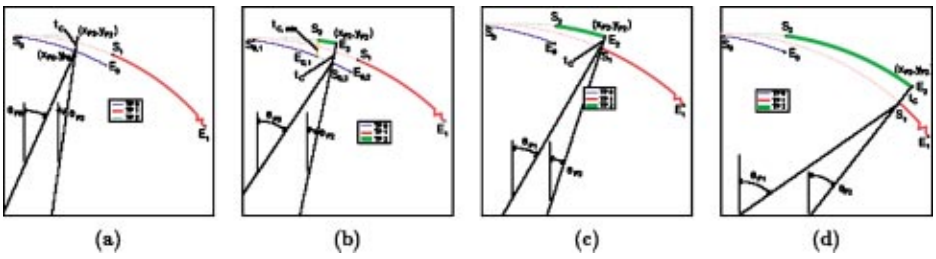

Fig. 3 Illustration of chip thickness computation for (*a*) chip thickness less than $t_{C,\min}$, (*b*) initial chip formation, (*c*) chip formation continuing across tool pass boundaries, and (*d*) results of tool pass

At the instance shown in Fig. 3(*c*), the current cutting edge has rotated until it has removed all of segment $S_{0,2}E_{0,2}$. Now, when θ_{F0} is computed, it is not found to intersect any of the current workpiece surface generated by tool pass 0, the arc segment S_0E_0. The value of θ_{F1}, the rotation angle corresponding to the first tool pass, is then computed. This is found to intersect the surface S_1E_1 and result in a chip thickness value that is greater than the minimum chip thickness. Because the chip thickness value is greater than the minimum chip thickness at the start of the surface intersection, the arc segment representing the surface is not split as surface S_0E_0 was in Fig. 3(*b*), but rather the value of S_1 is just modified as this surface is removed as shown in Fig. 3(*d*).

In summary, the developed chip-thickness computation algorithm is able to incorporate the effect of the minimum chip thickness on the chip formation process into the determination of the instantaneous chip thickness. Two separate cases are found to arise when computing the chip thickness. The instantaneous chip thickness may be larger than the minimum chip thickness when the current tool pass first intersects the surface from a previous revolution. This results in the starting point of the previous surface being modified as the tool rotates. The other case occurs whenever the instantaneous chip thickness becomes greater than the minimum chip thickness in between the start and end points for the previous surface. For this situation, the previous workpiece surface is split and the start point of the second segment modified as the tool rotates.

2.2 Orthogonal Force Model. Due to the fact that there exists a minimum chip thickness below which material will not be removed when machining with an edge-radiused tool [6,8,9], there are two separate mechanisms leading to forces in micromilling-chip formation and elastic deformation. In this paper, the chip formation force model is based on the orthogonal ploughing force model developed by Waldorf et al. [3]. When the chip thickness is too small to lead to chip formation, the elastic deformation forces are considered to be proportional to the interference volume between the tool and workpiece as was modeled by many other researchers [4,5,10–12].

2.2.1 Chip Formation Force Model. The force model during chip formation is based on the plane strain, slip-line plasticity model proposed by Waldorf et al. [3]. The forces along the shear plane in the cutting (C) and thrust (T) directions were found to be functions of the flow stress k, the shear angle φ, the rake angle α, the friction factor m, and the prow angle ρ [3]. In this work, due to the extreme nature of the frictional contact along the dead metal zone in front of the cutting edge, the friction factor is assumed to be a constant of 0.95. In Waldorf et al. [3], the prow angle was assumed to be 0 deg and the remaining parameters were estimated by measuring chips to determine the shear angle, performing large chip thickness cuts to estimate the flow stress from the forces by assuming the ploughing force components, $F_{P,C}$ and $F_{P,T}$, to be negligible, and by observing the rake angle at small chip thickness values with a video camera. Due to impracticalities in performing these approaches in microcutting experimentation, a different approach eliminating the need for physical experimentation is required.

In this work, a microstructure-level finite element program developed by Chuzhoy et al. [13] is used for this purpose. By performing simulations with multiple levels of tool and process geometry, functional relationships for the flow stress and the shear angle can be determined in terms of the appropriate parameters. Thus, micromilling force predictions can be determined for a wide range of the process and tool geometry conditions. Additionally, a more accurate estimation of the prow angle can be determined by observing the geometry of the workpiece surface during the FE simulations.

When machining at chip thickness values equal in magnitude and less than the edge radius, the rake angle affecting the machining process is more negative than the nominal rake α [14]. In order to quantify this effect, Manjunathaiah and Endres [15] used the average rake angle to investigate the influence of the edge radius on the machining process. The average rake angle α_{avg} is computed by first considering a line drawn between the lowest point on the cutting edge and a point on the rake face that is some multiple, ξ, of the chip thickness above the lowest point. The average rake angle is then computed to be the angle that this line makes with the normal to the cutting velocity,

$$\alpha_{avg}=\frac{\pi}{2}-\tan^{-1}\left(\frac{\xi t_C}{u}\right) \tag{7}$$

$$u=\begin{cases} -r_e\cos\left[\sin^{-1}\left(\dfrac{\xi t_C}{r_e}-1\right)\right]; & \xi t_C\leqslant r_e(1+\sin\alpha) \\ \dfrac{\xi t_C-r_e(1+\sin\alpha)}{\tan\left(\dfrac{\pi}{2}-\alpha\right)}-r_e\cos\alpha; & \xi t_C>r_e(1+\sin\alpha) \end{cases}$$

Manjunathaiah and Endres [15] reasoned that the value of ξ should be no less than 1 because that is the height of the uncut chip thickness on the tool. They assumed an upper bound on ξ based on the length of the sticking length of the chip on the rake face as proposed by Oxley [16]. In this paper, the average rake angle is computed and used for the rake angle in the model.

2.2.2 Elastic Deformation Force Model. When the chip thickness is less than the critical chip thickness, the elastic deformation forces are modeled as proportional to the volume of interference between the tool and the workpiece. Many researchers have employed this procedure in modeling the forces due to interference between the clearance face of the tool and the workpiece for the orthogonal cutting process [4,5], the turning process [11], and the endmilling process [10,12].

For the orthogonal cutting process, the interference volume is shown as the shaded region in Fig. 4. The geometry of the cutting edge is shown in the figure. The cutting edge is represented as having a radius equal to r_e. The clearance angle of the tool is represented by γ_0. For a given penetration depth p, the volume of interference is computed using Eq. (8),

$$V_{\text{int}}=\begin{cases} wr_e^2(\theta_1-0.5\sin 2\theta_1) & p\leqslant r_e(1-\cos\gamma_0) \\ \dfrac{w}{2}\left[r_e^2(\theta_1+\gamma_0)-r_e(r_e-p)(\sin\theta_1+\sin\gamma_0)+\dfrac{(p-r_e(1-\cos\gamma_0))^2}{\tan\gamma_0}\right] & \text{else} \end{cases}$$

$$\theta_1=\cos^{-1}\left(1-\frac{p}{r_e}\right) \qquad (8)$$

$$\theta_2=\gamma_0$$

The penetration depth quantitatively is identical to the chip thickness t_C computed in Eq. (6) for cases in which $t_C<t_{C,\min}$, and is denoted differently to emphasize that no chip is formed in these situations. The elastic deformation forces can then be computed,

$$dF_T=K_{\text{int}}V_{\text{int}}$$
$$dF_C=\mu_{\text{int}}dF_T \qquad (9)$$

where K_{int} and μ_{int} are the interference force constant and the coefficient of friction for the elastic deformation force model.

2.3 Transformation to Endmilling Geometry. For endmilling force prediction, the orthogonal forces need to be transformed into the three-dimensional Cartesian coordinate system shown in Fig. 5 with the inclination angle *i*. The inclination angle is the angle that the cutting edge makes with the normal to the cutting velocity. For the cases in which a chip is formed, the orthogonal thrust force F_T simply becomes the radial force F_{rad}. The cutting force is broken into two components, the longitudinal force F_{lon} and the tangential force $F_{\tan}$ by the inclination angle as in Eq. (10),

$$dF_{rad}=dF_T$$
$$dF_{lon}=dF_C\sin i \qquad (10)$$
$$dF_{\tan}=dF_C\cos i.$$

For the case in which no chip is formed, the elastic deformation forces are computed as

$$dF_{rad}=dF_T$$
$$dF_{\tan}=dF_C \qquad (11)$$

Since the relative motion between the cutting edge and the workpiece is in the tangential direction, the friction force is assumed to act solely in that direction.

The total endmilling forces are then found by computing the forces for each axial slice of the endmill and for each flute using the appropriate force model based on the instantaneous chip thickness of each axial slice. The differential radial, longitudinal and tangential forces from either Eq. (10) or (11) for each slice are then transformed into the global Cartesian coordinate system (recall Fig. 1),

$$\begin{bmatrix} dF_X \\ dF_Y \end{bmatrix}=\begin{bmatrix} -\sin\theta & \cos\theta \\ \cos\theta & \sin\theta \end{bmatrix}\begin{bmatrix} dF_{rad} \\ dF_{lon} \end{bmatrix}$$
$$dF_Z=dF_{lon} \qquad (12)$$

The forces due to all slices are then added to determine the total forces,

$$F_X=\sum_{N_{flutes}}\sum_{z} dF_X$$
$$F_Y=\sum_{N_{flutes}}\sum_{z} dF_Y \qquad (13)$$
$$F_Z=\sum_{N_{flutes}}\sum_{z} dF_Z$$

3 Model Calibration

In order to use the model to predict forces in the micromilling of ductile irons, material-dependent model parameters need to be determined for the main metallurgical phases of the material, ferrite and pearlite. For each metallurgical phase, the chip formation

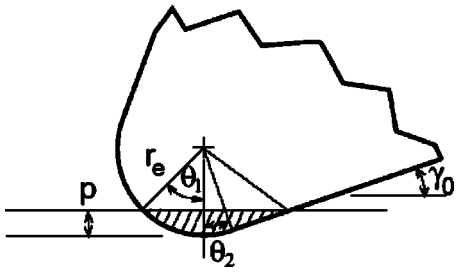

Fig. 4 Schematic showing interference volume

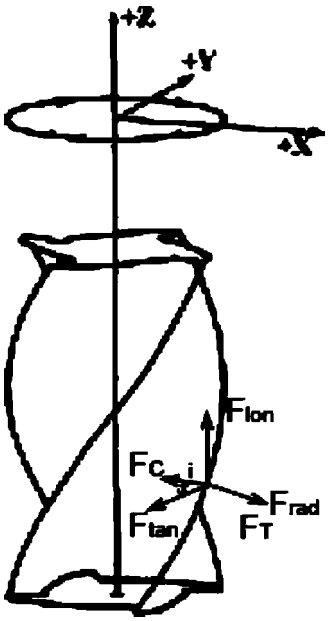

Fig. 5 Relation of endmilling forces to orthogonal machining forces

Table 1 FE simulation conditions

Variable	Levels
Material	Pearlite and Ferrite
Edge radius	2 and 7 μm
Rake angle	0 and 7°
Clearance angle	5 and 11 deg
Chip thickness	0.1, 0.25, 0.5, 1, 2, and 3 μm

force model parameters (k and φ) and the elastic deformation force model parameters (K_{int} and μ_{int}) need to be found in addition to the minimum chip thickness values found in Part I [1]. These model parameters were all determined via a microstructure-level finite element (FE) simulation developed by Chuzhoy et al. [13].

The finite element simulation developed by Chuzhoy et al. [13] was used to simulate the orthogonal machining of the ferrite and pearlite phases to be used here in the prediction of ductile iron micromilling forces. All simulations were performed for a cutting velocity of 200 m/min and a width of cut of 1 mm. The rake angle α, the clearance angle γ_0, the edge radius r_e, and the chip thickness t_C were varied over the conditions listed in Table 1.

In order to calibrate the parameters in the chip formation and the elastic deformation force models, the steady-state forces from the FE simulations were determined. These forces were then divided into two groups determined by whether or not the chip thickness is greater than the minimum chip thickness values of $0.20r_e$ and $0.35r_e$ for the pearlite and ferrite, respectively, as determined in Part I [1]. For those simulation conditions with a chip thickness below the minimum chip thickness, the interference volume was computed with Eq. (8) and the elastic deformation force model coefficients K_{int} and μ_{int} computed. Since it is reasonable to assume that the elastic deformation force model coefficients are constant and proportional to the interference volume [4,17], the interference force constants K_{int} are found to be 3.8e6 and 3.2e6 [N/mm^3], and the coefficients of friction are found to be 0.6 and 0.5 for ferrite and pearlite, respectively, by averaging the individual values computed for the simulations resulting in no chip formation.

For those simulations with a chip thickness greater than the minimum chip thickness, the average rake angle was computed using Eq. (7) using ξ=1.5, the midpoint in the range of ξ as discussed in Manjunathaiah and Endres [15]. For each of the simulation conditions, the flow stress and shear angle were then determined by solving the cutting and thrust force equations in Waldorf et al. [3] and are plotted in Figs. 6(*a*) and (*b*). Based on the appearance of the plots, linear relationships were fit for the shear angle as

$$\phi_{Ferrite} = 26.66 + 0.30\alpha_{avg}$$
$$\phi_{Pearlite} = 31.48 + 0.32\alpha_{avg} \tag{14}$$

and are plotted along with the computed shear angle values in Figs. 6(*a*) and (*b*). This linear trend of the shear angle with the rake angle is not unexpected due to the early work of Merchant [18] and Lee and Shaeffer [19], in which it was assumed that a linear relationship existed between the rake angle and the shear angle. The computed flow stress values for ferrite and pearlite are shown in Figs. 7(*a*) and (*b*). There are more points in the plots for the pearlite than for ferrite in Figs. 6 and 7 due to the lower minimum chip thickness for pearlite of 0.40 μm compared to 0.70 μm for ferrite. The flow stress values are assumed to be constant based on the work of Shaw and Finnie [20], which showed that the flow stress is fairly constant over a range of feeds. The average values for the ferrite and pearlite were computed to be 525 and 650 MPa, respectively.

The trends in the calibration parameters can be explained in terms of the material behavior of the ferrite and pearlite phases. The shear angle and average rake angle relationships for ferrite and pearlite have a similar slope for the average rake angle dependence since both materials are ferrous materials. The shear angles are lower for the ferrite phase due to its increased ductility and the increased significance of the ploughing forces in ferrite machining. The flow stress of pearlite is determined to be greater than the flow stress of ferrite as expected due to the greater strength of pearlite.

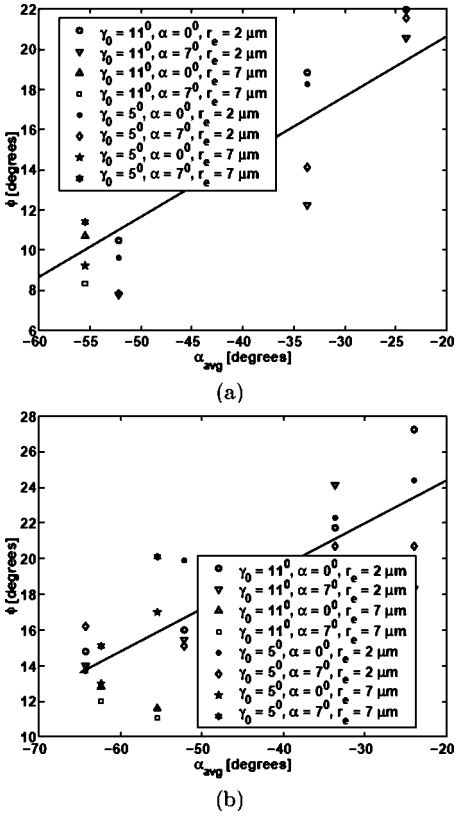

Fig. 6 Shear angle as a function of average rake angle for (*a*) ferrite and (*b*) pearlite

4 Model Validation

To determine the effectiveness of using the enhanced model to predict the forces in the micro-endmilling, experiments on single phase materials, ferrite and pearlite, and two different ductile irons were performed using the conditions in Table 2 as described in Part I of this paper [1]. A spindle speed of 120,000 rpm, corresponding to a cutting velocity of 200 m/min, was chosen for the experiments and the force signals was sampled at 40 kHz. The *Y*-force signal was found to have the best signal-to-noise ratio during cutting and noncutting investigations and will be the force signal that is used to validate the model.

The cutting forces were predicted by using the model described in Section 2 and the force model parameters determined for the ferrite and pearlite materials in Section 3 of this paper. Based on observations of the experimental force data, the parallel axis offset was assumed to be 0 μm in the simulations. The results from these simulations were then compared to the experimental data using two metrics. First, the peak-to-valley forces were considered. This will show the ability of the model and the calibration strategy to accurately predict the magnitude of the forces for both the ferrite and pearlite as well as for the ductile iron samples. Then, the nature of the frequency spectra was considered. The presence or absence of certain frequency components in the predicted data was compared to the experimental data.

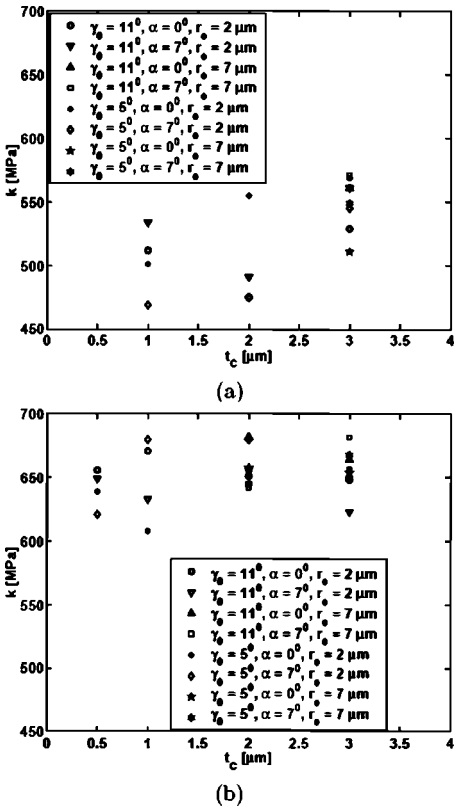

Fig. 7 Flow stress as a function of chip thickness for (*a*) ferrite and (*b*) pearlite

4.1 Force Magnitude

4.1.1 Ferrite and Pearlite Forces. The peak-to-valley *Y* forces are plotted in Fig. 8 for both the experimental and simulated ferrite and pearlite forces. Overall, the model is shown to accurately predict the magnitude in the ferrite and pearlite force data. With a few exceptions excluded and to be discussed later, the average percent error for the force magnitudes is computed to be 18.5% and 18% for the pearlite and ferrite force magnitudes, respectively.

The following experimental trends are also well predicted by the model. In Fig. 8, it is clearly seen that the peak-to-valley forces are larger for the 100 μm axial depth of cut slots compared to the 50 μm axial depth of cut slots. The difference between the two depths of cut are well predicted by the model. Also, the forces for the slots machined with the 5 μm edge-radiused endmills are larger than those with the 2 μm edge-radiused tool. This change in the peak-to-valley force, as the cutter edge radius increases, is more pronounced for the ferrite than for the pearlite. This edge radius effect and interaction effect between the edge radius and the material is accurately predicted by the model. Even though the maximum chip thickness increases by a factor of 12 as the feed rate is increased from 0.25 to 3.0 μm/flute, the force magnitude increases only by a factor of 2–3 for the 2 μm edge radius pearlite forces and stays virtually the same for the 5 μm edge radius ferrite forces as seen in both the predicted and experimental data. The magnitude of the ferrite forces are very similar to the magnitude of the pearlite forces for the 2 μm edge-radiused endmills. However, the ferrite forces are larger than the pearlite forces for the 5 μm edge-radiused endmills due to the increased significance of ploughing with the more ductile ferrite.

Table 2 Experimental design

Test	r_e (μm)	ADOC (μm)	f_t (μm/flute)
1	2	50	0.25
2	2	50	0.5
3	2	50	1.0
4	2	50	2.0
5	2	50	3.0
6	2	100	0.25
7	2	100	0.5
8	2	100	1.0
9	2	100	2.0
10	2	100	3.0
11	5	50	0.25
12	5	50	0.5
13	5	50	1.0
14	5	50	2.0
15	5	50	3.0
16	5	100	0.25
17	5	100	0.5
18	5	100	1.0
19	5	100	2.0
20	5	100	3.0

4.1.2 Ductile Iron Forces. In order to predict the micromilling forces for the machining of the two ductile iron specimens, a mapping of the microstructure had to first be created. The same microstructural mappings described in Vogler et al. [2] were created.

The peak-to-valley *Y* forces were then computed for both the experimental and simulated ductile iron forces and are shown in Figs. 9(*a*)–9(*d*). Even though the calibration was performed on only the ferrite and pearlite and not on the ductile irons, the magnitude of the forces are predicted very well. Similar trends with processing conditions are observed in the multiphase ductile iron data as were seen in the ferrite and pearlite data presented earlier. The average percent error between the experimental and simulated peak-to-valley forces was calculated to be 20% and 14% for the pearlitic and ferritic ductile iron force magnitudes, respectively. As was demonstrated earlier in Vogler et al. [2] and reinforced with this data, the approach of using the calibrated force models for the individual microstructural constituents is able to accurately predict the force magnitudes for multiphase materials given an appropriate geometric model of the microstructure.

4.1.3 Sensitivity of Edge Radius Variation on the Force Prediction. Given the measurement procedure described in Part I [1] for the determination of the cutter edge radius, it is believed that there exists some variability in the cutting edge radius of the endmills within the endmills selected to have a 2 μm nominal edge radius endmills and within those endmills selected to have a 5 μm nominal edge radius. In this section, the effect of this variation on the cutting force prediction will be discussed.

As seen in Figs. 8 and 9, there are several test conditions for the which the experimental force data is significantly above or below the simulated force magnitude. This appears to be related to the variation in the tooling used for the experiments. For example, the following four conditions were machined with the same, nominally 5 μm edge-radiused endmill:

1. Ferrite, 100 μm depth of cut, 3.0 μm/flute feed
2. Pearlite, 100 μm depth of cut, 0.5 μm/flute feed
3. Ferritic DI, 50 μm depth of cut, 0.5 μm/flute feed
4. Pearlitic DI, 50 μm depth of cut, 2.0 μm/flute feed

Closer inspection of the predicted and experimental force magnitudes reveals that the force magnitude was overpredicted for all four cases. Therefore, it is believed that the edge radius along the cutting edge was less than the 5 μm observed at the end of the endmill.

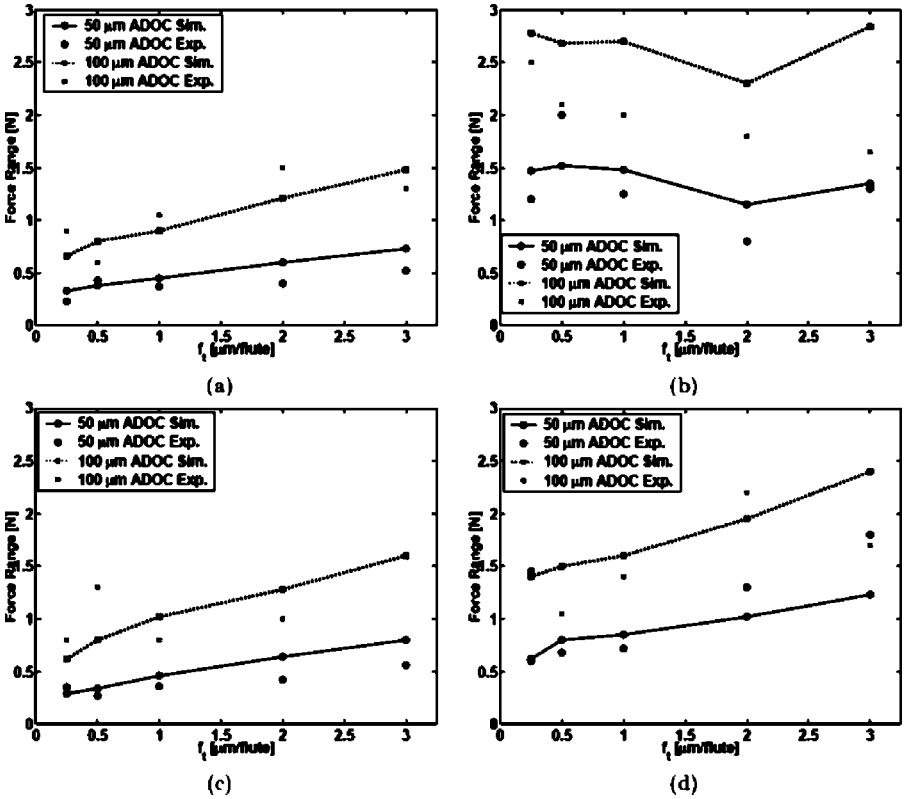

Fig. 8 Experimental and predicted peak-to-valley forces for (*a*) ferrite, 2 μm edge radius; (*b*) ferrite, 5 μm edge radius; (*c*) pearlite, 2 μm edge radius; and (*d*) pearlite, 5 μm edge radius

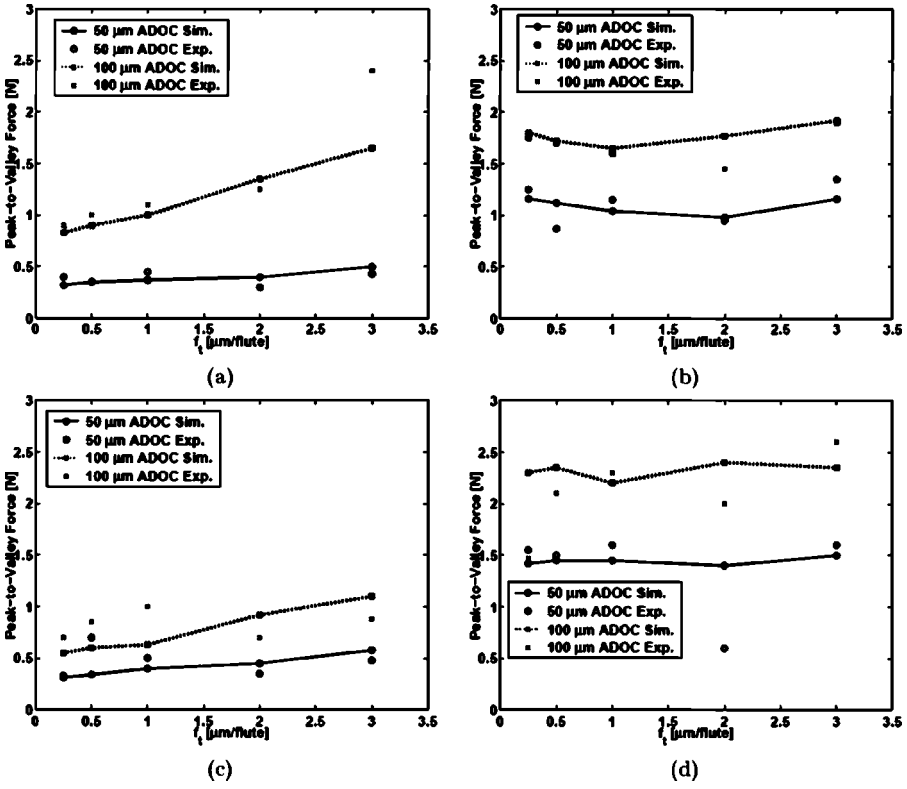

Fig. 9 Experimental and predicted peak-to-valley forces for (*a*) ferritic DI, 2 μm edge radius; (*b*) ferritic DI, 5 μm edge radius; (*c*) pearlitic DI, 2 μm edge radius; and (*d*) pearlitic DI, 5 μm edge radius

Table 3 Sensitivity of edge radius

Example #	Nominal r_e	% Error $w/r_e=5$	% Error $w/r_e=4$
1	5	42	21
2	5	30	10
3	5	22	2
4	5	57	20
5	2	−24	−6
6	2	−63	−6
7	2	−45	−20
8	2	−59	−5

The opposite behavior is observed for another nominally 2 μm edge-radiused endmill used to machine the following experiment conditions:

1. Ferrite, 100 μm depth of cut, 2.0 μm/flute feed
2. Pearlite, 100 μm depth of cut, 0.5 μm/flute feed
3. Ferritic DI, 100 μm depth of cut, 3.0 μm/flute feed
4. Pearlitic DI, 100 μm depth of cut, 1.0 μm/flute feed

For all four experiment conditions machined with this tool, the forces are under-predicted by the model.

Simulations were performed for endmills with edge radii of 3 and 4 μm in order to determine the predicted force magnitudes for a range of edge radii. For conditions 1–4 above, the percent error for the simulations using a 5 μm edge radius and using a 4 μm edge radius are listed in Table 3. The percent errors are much less for the simulations using a 4 μm edge radius, indicating that the endmill used for those experiments may be more accurately represented as having a 4 μm edge radius. A similar comparison is performed for conditions 5–8. The percent errors for those conditions are much less for the simulations using the 3 μm edge radius than for the simulations using the estimated 2 μm edge radius. It is clear that at the size scales employed in the micromilling process, the cutter edge radius has a significant effect on the cutting force system.

4.2 Frequency Spectra Results. The influence of the minimum chip thickness on the micromilling forces can also be observed in the micromilling force spectrum. Figure 10 shows the simulated and experimental *Y*-forces and their spectra. In addition to the tooth passing frequency of 4 kHz, there are other frequencies in both spectra. Both spectra contain a significant component at 7 kHz. Also, there is a significant force component at 1.3 kHz in the simulated spectrum, which although less pronounced, is also present in the experimental spectrum. The frequency behavior of the 1.3 kHz component can also be observed in the time domain. In both the simulated and the experimental data, a stepping behavior in the forces every three tooth passes can be observed. As the feedrate is increased, however, the frequency components less than 4 kHz disappear from the force spectra. Figure 11 shows the experimental and simulated Y-forces and spectra for pearlite test condition 10. In these spectra, the dominant peaks are the tooth passing frequency (4 kHz) and their harmonics. When observing the time domain force signals, no evidence of stepping in the magnitude of the forces is present. The relationship between the minimum chip thickness and the feed rate that causes this stepping behavior will be discussed in Section 5.

The 0 μm value of the parallel axis offset runout used in the simulations can also be validated by considering the frequency spectrum of the experimental forces. Kline and DeVor [21] found that cutter runout results in a peak in the spectrum at a frequency equal to the spindle frequency. Runout can also be identified by observing a repeatable variation in the peaks in the force signal. As shown clearly in Fig. 11(*b*), there is no frequency component

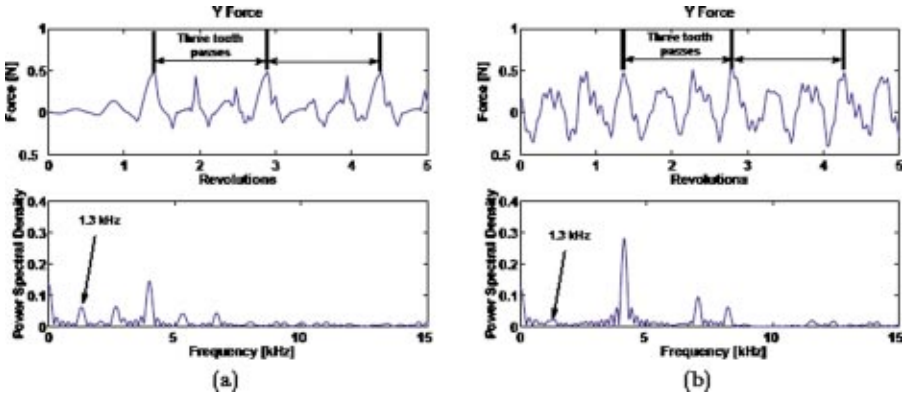

Fig. 10 (*a*) Simulated and (*b*) experimental *Y* forces and spectra for pearlite test 6

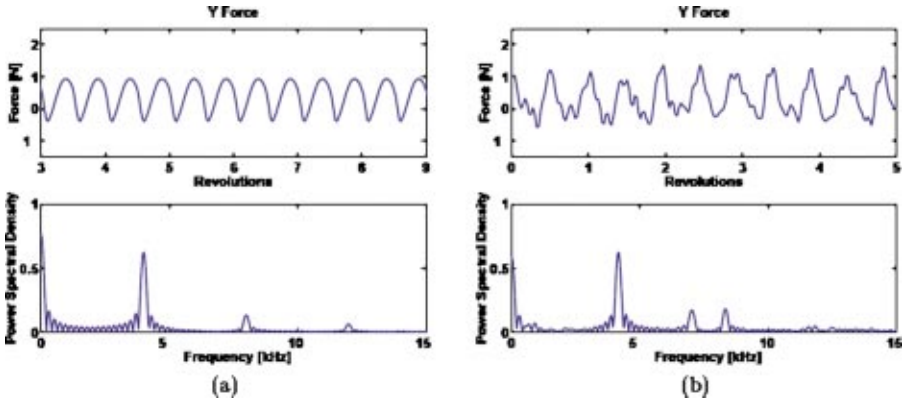

Fig. 11 (*a*) Simulated and (*b*) experimental *Y* forces and spectra for pearlite test 10

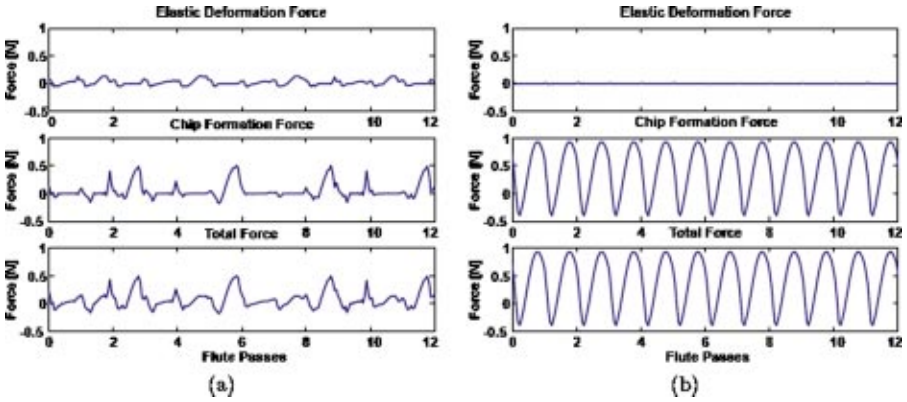

Fig. 12 Decomposition of forces for (*a*) pearlite test 6 and (*b*) pearlite test 10

at the spindle frequency of 2 kHz, nor is there any repeatable variation in the experimental force signal. Therefore, there is no evidence of runout in these experiments.

5 Discussion

5.1 Effect of Material Behavior. The trends observed during model validation can be explained by considering the effects of the workpiece material behavior on the force system in light of the slip-line model. Ferrite is a more ductile material than pearlite and, therefore, is more affected by ploughing. Therefore, the increase in edge radius has a much larger effect on ferrite than pearlite. For the 2 μm edge-radiused endmill, the forces between ferrite and pearlite are very similar in magnitude. However, with the 5 μm edge-radiused endmill, the forces are much larger for ferrite than pearlite due to the increased ploughing forces for ferrite. These results indicate that the material ductility can more significantly affect the magnitude of the forces in micromilling than either the flow stress or the hardness. Pearlite has both a larger flow stress and a higher hardness, yet the forces are comparable in magnitude or lower than the ferrite micromilling forces when machined at 200 m/min.

5.2 Effect of Minimum Chip Thickness. The relatively small change in force magnitude with feedrate is explained by both the minimum chip thickness effect and the significance of ploughing in the micromilling force process. First, for small values of the feedrate, the maximum chip thickness during one tooth pass is less than the minimum chip thickness for the material, $0.20r_e$ and $0.35r_e$ for the pearlite and ferrite, respectively. For the 2 μm edge-radiused endmills the actual minimum chip thickness values are 0.4 and 0.7 μm, and for the 5 μm edge-radiused endmills, the actual minimum chip thickness values are 1.0 and 1.75 μm. Thus, a chip will not be formed during every tooth pass, resulting in a chipload during chip formation that is greater than that expected without the minimum chip thickness effect. In addition to the minimum chip thickness effect, the significance of ploughing has an effect on the pattern of the force magnitudes with feedrate. As the chip thickness increases, the average rake angle increases. This results in a larger shear angle as shown in the calibration plots of Figs. 6(*a*) and 6(*b*). Larger shear angles lead to shorter shear plane lengths and relatively lower forces.

The minimum chip thickness also explains the stepping behavior in the forces at lower feed rates. Until the instantaneous chip thickness increases to be larger than the minimum chip thickness, the workpiece material is just elastically deformed. Therefore, the forces increase with each tool pass until the chip thickness is greater than the minimum chip thickness. At this point, a chip is formed and the material is removed. This process then repeats, resulting in a chip being formed every *n* tool pass. This process of a chip being formed every *n* tool pass was first proposed by Kim et al. [8] during micromilling of brass and aluminum and is now accurately predicted by the enhanced micromilling models developed in this paper. This phenomenon is clearly observed in Fig. 12(*a*) in which the predicted *Y* force for pearlite test 6 is decomposed into a component due to the elastic deformation and a component due to chip formation. Clearly, the majority of the chip formation force occur every three tool passes, while the elastic deformation forces gradually build every three passes until a chip is formed. This stepping behavior in the forces for the low feed rate case can be contrasted with the force decomposition for the high feedrate case in Fig. 12(*b*). For large values of the feedrate relative to the minimum chip thickness, the forces are due almost entirely to chip formation.

5.3 Effect of Runout. The presence of parallel axis offset runout results in behavior that is similar to the minimum chip thickness. At low values of runout relative to the feedrate, the runout may cause one flute not to intersect the workpiece at any time. The force signal for this case has zero force signals for segments corresponding to the missing tool pass as shown in Fig. 13(*a*) for a pearlite simulation using the conditions of test 6 with 1 μm runout. Due to the runout, a chip is now formed every four tool passes compared to every three tool passes without runout. Figure 13(*b*) shows the force decomposition for a pearlite simulation using the conditions of test 10 with 1 μm runout. Although the total force exhibits a stepping pattern every two passes, it is found that the force is almost entirely due to chip formation.

5.4 Effect of Workpiece Microstructure. In the previous work of Vogler et al. [2], frequency components in the force spectra during the machining of ductile iron were found to correlate with the spacing of the ferritic grains in the multiphase microstructure. These frequency components are not found in the ductile iron experimental force spectra presented here for several reasons. First, as these frequency components are the result of the cutting edge moving among the phases, the frequency is proportional to the cutting velocity. At the 120,000 rpm conditions used in these experiments, the expected location of these frequency components would be between 40 and 60 kHz, much beyond the bandwidth of the load cell used to collect the forces. Second, as found in the FE simulations and observed in the ferrite and pearlite micromilling force data, at a 200 m/min cutting velocity, the difference in magnitude between the ferrite and pearlite forces is much less than in the forces at 30,000 rpm (50 m/min cutting velocity) [2]. This result is supported by the model characterization performed by Chuzhoy et al. [22] for both ferrite and pearlite in which a strong strain-rate dependency on the stress was found for the ferrite samples.

This is not to say that the current model is incapable of predicting these workpiece microstructure-based force variations. A flow stress of 350 MPa for ferrite is representative for machining at the

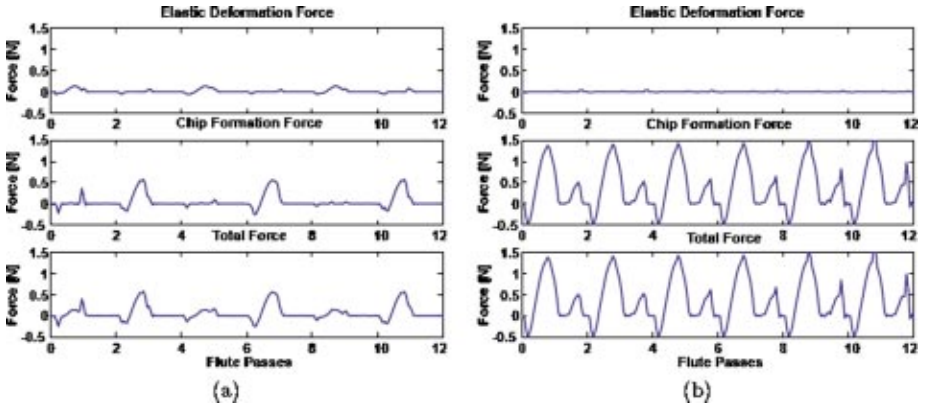

Fig. 13 Decomposition of forces with 1 μm runout for (*a*) pearlite test 6 and (*b*) pearlite test 10

50 m/min cutting velocity used in the previous work [2]. Using this flow stress for the ferrite in the pearlitic ductile iron simulation, the *Y* force and its spectrum with the tooth passing frequency removed are generated as shown in Fig. 14. In this figure, the peaks in the spectrum around 44 kHz are due to the average spacing of the ferrite grains in the workpiece microstructure and are close in magnitude to the second harmonic of the tooth passing frequency. Therefore, the effect of the microstructure is to produce higher frequency force variations at frequencies corresponding the distance between phases in the workpiece. The presence of these higher frequency force variations is also supported by the observed characteristics of the surface in Part I [1]. Miniature burrs were observed on the slot floor at a spacing related to the phase boundaries in the microstructure. These wavelengths were also prominent in the spectra of the surface profiles for the slot floor centerlines. Therefore, there is evidence in both the simulated and the experimental force and the surface data that the geometry of the multiphase microstructure has an important effect on the micromilling process.

5.5 Previous Micro-Milling Force Model [2] Revisited. The enhanced force model presented in this paper allows for the phenomenological study of the effects of the edge radius on the micromilling process. The trends that can now be explained by the enhanced model, such as the variation of the force magnitude with feed rate, were also present in the previous work [2]. Although the previous model was able to accurately predict the magnitude of the forces, it did not have the ability to phenomenologically explain the behavior of the micromilling forces with process conditions and tool geometry. This behavior was simply lumped in the coefficients of the force model through the calibration procedure employed. The enhancements made to the model in this paper extend the predictive capability of the micromilling force model by explicitly including the effects of the cutter edge geometry and further the understanding of the micromilling process.

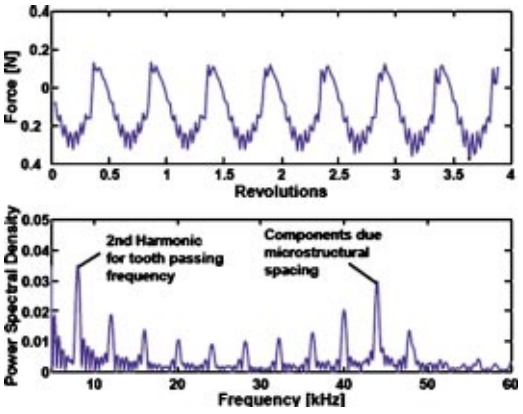

Fig. 14 *Y* force and filtered spectrum to show effect of workpiece microstructure on force system

The results of this research indicate that care must be taken to properly select the cutting conditions in micro-endmilling operations. Reducing the feed rate does not linearly decrease the cutting forces, and, therefore, the power required to remove a certain amount of material may increase as the feedrate is reduced. The miniature endmill deflection is not always minimized by reducing the feed rate because the forces do not always decrease. Additionally, using feed rates significantly less than the minimum chip thickness results in frequencies less than the tooth-passing frequency. These lower frequencies are more likely to be near the dominant vibration modes of the manufacturing equipment than the tooth-passing frequencies when machining with 100,000+ rpm spindle speeds. Increasing the feed rate so that only the tooth passing frequency and its harmonics are present may shift the forced vibration to frequencies larger than the dominant vibration modes of the structures. These trends indicate that increasing the feedrate may improve the accuracy of the micro-endmilling process over some range of feed rates.

6 Conclusions

Based on the micromilling experimentation and modeling efforts presented in Part II of this paper, the following conclusions can be drawn:

1. A cutting force model was developed for micromilling that includes the effects of machining with a cutting edge radius equal in magnitude or larger than the chip thickness. A new chip thickness computation algorithm was developed in order to consider that a chip is not always formed when the tool and workpiece intersect. Additionally, the minimum chip thickness requires that two separate force models be included to handle the situations in which a chip is and is not formed.
2. Finite element simulations were performed to calibrate the parameters of the micromilling force models for both the ferrite and pearlite phases. The average interference force constants and coefficients of friction were determined for the elastic deformation force model. The average flow stress and the linear shear angle and average rake angle relationships were calibrated for the chip formation force model. The prow angle used in the chip formation force model was also observed from the FE simulations.
3. Predictions from the model compared favorably to experiment results in terms of the magnitude of the forces. Force

magnitudes were predicted with average percent errors of 18.5% and 18% for machining pearlite and ferrite, respectively. Ductile iron forces were predicted with an average percent error of 20% using the calibration for the ferrite and pearlite and appropriate microstructure maps for the heterogeneous materials. For a 12-fold increase in the chipload, the magnitude of the cutting forces increased less than threefold for the range of cutting conditions tested.

4. The frequency spectra of the forces were found to contain a component that is a subharmonic of the tooth-passing frequency at feedrates less than the minimum chip thickness and appears as a stepping behavior of the forces in the time domain. A decomposition of the simulated forces showed that this stepping behavior is the result of the interference between the tool and workpiece increasing during subsequent revolutions until the instantaneous chip thickness is greater than the minimum chip thickness.
5. The simulations and model predictions showed that the forces are more sensitive to the edge radius when machining ferrite than when machining pearlite, due to both the minimum chip thickness and the increased ductility of the ferrite material behavior that increases the ploughing forces.

Acknowledgments

The authors gratefully acknowledge the financial support of the National Science Foundation through Grant No. DMII01-14717. The authors would like to thank Dr. Leo Chuzhoy of Caterpillar, Inc., for the workpiece material, and Sunghyuk Park for his assistance in performing the FE simulations.

References

[1] Volger, M. P., DeVor, R. E., and Kapoor, S. G., 2004, ''On the Modeling and Analysis of Machinery Performance in Micro-Endmilling, Part I: Surface Generation,'' ASME J. Manuf. Sci. Eng., **126**(4), pp. 695–705.
[2] Vogler, M. P., DeVor, R. E., and Kapoor, S. G., 2003, ''Microstructure-Level Force Prediction Model for Micro-Milling of Multi-Phase Materials,'' ASME J. Manuf. Sci. Eng., **125**, pp. 202–209.
[3] Waldorf, D. J., DeVor, R. E., and Kapoor, S. G., 1998, ''A Slip-Line Field for Ploughing During Orthogonal Cutting,'' ASME J. Manuf. Sci. Eng., **120**, pp. 693–699.
[4] Wu, D. W., 1989, ''A New Approach of Formulating the Transfer Function for Dynamic Cutting Processes,'' ASME J. Eng. Ind., **111**, pp. 37–47.
[5] Endres, W. J., DeVor, R. E., and Kapoor, S. G., 1995, ''A Dual Mechanism Approach to the Prediction of Machining Forces, Part I: Model Development,'' ASME J. Eng. Ind., **117**, pp. 526–533.
[6] Shimada, S., Ikawa, N., Tanaka, H., Ohmuri, G., Uchikoshi, J., and Yoshinaga, H., 1993, ''Feasibility Study on Ultimate Accuracy in Microcutting Using Molecular Dynamics Simulation,'' CIRP Ann., **42**, pp. 91–94.
[7] Yuan, Z. J., Zhou, M., and Dong, S., 1996, ''Effect of Diamond Tool Sharpness on Minimum Cutting Thickness and Cutting Surface Integrity in Ultraprecision Machining,'' J. Mater. Process. Technol., **62**, pp. 327–330.
[8] Kim, C.-J., Bono, M., and Ni, J., 2002, ''Experimental Analysis of Chip Formation in Micro-Milling,'' Trans. NAMRI/SME, **XXX**, pp. 247–254.
[9] Weule, H., Huntrup, V., and Tritschler, H., 2001, ''Micro-Cutting of Steel to Meet New Requirements in Miniaturization,'' CIRP Ann., **50**, pp. 61–64.
[10] Elbestawi, M. A., Ismail, F., Du, R., and Ullagaddi, B. C., 1994, ''Modeling Machining Dynamics Including Damping in the Tool-Workpiece Interface,'' ASME J. Eng. Ind., **116**, pp. 435–439.
[11] Shawky, A. M., and Elbestawi, M. A., 1997, ''An Enhanced Dynamic Model in Turning Including the Effect of Ploughing Forces,'' ASME J. Manuf. Sci. Eng., **119**, pp. 10–20.
[12] Narayanan, K., Ranganath, S., and Sutherland, J. W., 1997, ''A Dynamic Model of the Cutting Force System in Peripheral Milling Characterizing the Effects of Flank Face Interference,'' Proc. of ASME Annual Meeting, ASME, New York, MED Vol 6-2, pp. 143–151.
[13] Chuzhoy, L., DeVor, R. E., Kapoor, S. G., and Bammann, D. J., 2002, ''Microstructure-Level Modeling of Ductile Iron Machining,'' ASME J. Manuf. Sci. Eng., **124**, pp. 162–169.
[14] Nakayama, K., and Tamura, K., 1968, ''Size Effect in Metal-Cutting Force,'' ASME J. Eng. Ind., **90**, pp. 119–126.
[15] Manjunathaiah, J., and Endres, W. J., 2000, ''A Study of Apparent Negative Rake Angle and Its Effects on Shear Angle During Orthogonal Cutting With Edge-Radiused Tools,'' Trans. NAMRI/SME, **XXVIII**, pp. 197–202.
[16] Oxley, P. L. B., 1989, *The Mechanics of Machining: An Analytical Approach to Assessing Machinability*, John Wiley and Sons, New York.
[17] Shaw, M. C., and DeSalvo, D. J., 1970, ''A New Approach to Plasticity and Its Application to Blunt Two-Dimensional Indenters,'' Trans. ASME, Ser. C: J. Heat Transfer, **92**, pp. 469–479.
[18] Merchant, M. E., 1944, ''Basic Mechanics of the Metal-Cutting Process,'' ASME J. Appl. Mech., **11**, pp. 168–175.
[19] Lee, E. H., and Shaffer, B. W., 1951, ''The Theory of Plasticity Applied to a Problem of Machining,'' ASME J. Appl. Mech., **18**, pp. 405–413.
[20] Shaw, M. C., and Finnie, I., 1955, ''The Shear Stress in Metal Cutting,'' Trans. ASME, **77**, pp. 115–126.
[21] Kline, W. A., and DeVor, R. E., 1983, ''The Effect of Runout on Cutting Geometry and Forces in End Milling,'' Int. J. Mach. Tool Des. Res., **23**, pp. 123–140.
[22] Chuzhoy, L., DeVor, R. E., Kapoor, S. G., Beaudoin, A. J., and Bammann, D. J., 2001, ''Machining Model of Ductile Iron and Its Constituents, Part I: Estimation of Material Model Parameters and Their Validation,'' *Proc. of ASME Manufacturing Engineering Div.*, ASME, New York, MED Vol. 12.